Modeling Solar Eruptions of Magnetic Flux Ropes with New Techniques

Predictive Science Inc.

Viacheslav S. Titov, Cooper Downs, Tibor Török, Jon A. Linker

Predictive Science Inc., San Diego, CA

Abstract. We demonstrate our new techniques for modeling solar eruptions in magnetic configurations that contain magnetic flux ropes (MFRs). The magnetic field of the configuration is represented as a sum of the potential magnetic field produced by the photospheric sources and the MFR field with a vanishing normal component at the boundary. Using observations we first identify an approximate axis path and radius of the MFR with an assumed circular cross-section. Then we determine the magnetic field generated by axial and azimuthal currents of the modeled MFR and their mirror images about the surface boundary by means of the so-called regularized Biot-Savart laws (RBSLs). The corresponding value of the total current and the axis path are iteratively determined from the minimization of magnetic forces acting on the MFR. Thus optimized magnetic configuration is relaxed then in line-tied zero-beta MHD simulations toward a force-free equilibrium. Finally, we energize the obtained MFR equilibrium by applying our newly developed ``helicity pumping" method that brings the configuration to an unstable state through a series of small MHD perturbations and relaxations without changing the normal magnetic field at the boundary.

We illustrate these techniques by applying them to the modeling of the February 13, 2009 CME event. We find that, in spite of the bipolar character of the external field, the MFR eruption is sustained from the onset by two reconnection processes. The first, which we refer to as breakthrough reconnection, is analogous to breakout reconnection in quadrupolar configurations. It occurs at a quasi-separator inside a current layer that wraps around the erupting MFR. The second process is the classical tether-cutting (flare) reconnection, which develops at the second quasi-separator inside a vertical current layer that is formed below the erupting MFR. Both reconnection processes work in tandem with the magnetic forces of the unstable MFR to propel it through the overlying ambient field. At a later stage of the eruption, breakout reconnection is also triggered to facilitate the motion of the erupting structure through the global background field.

Our results illustrate how such methods can be extremely useful for theoretical studies of solar eruptions as well as data-constrained modeling of observed events.

STEREO/EUVI EUV images of the PEC of the **2009 February 13 CME** (left). (b) The yellow and red lines show the initial and optimized axis paths, respectively. Q-maps are shown for optimized MFR (before MHD relaxation). Only high-Q lines with $\log_{10} Q \geq 4.0$ (sky-blue and crimson for negative and positive polarities, respectively) are shown on top of the photospheric B_r-distribution (gray shaded). Q-maps are depicted also in the central cross-section of the optimized PECs (inverted grayscale palette with fully transparent colors at $\log_{10} Q < 2.0$). The numerical grid is outlined at the boundary.

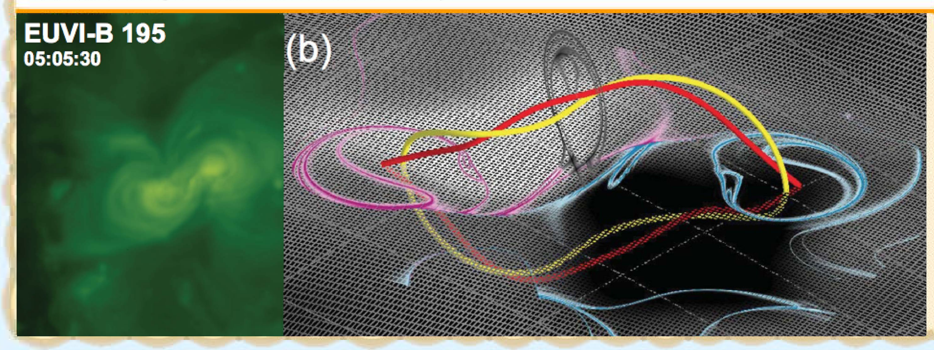

1 Estimate axis path $\mathbf{R}(l)$ and radius a of the MFR from observations.

MFR with a circular cross-section of radius $a(l)$ and coronal and subphotospheric axis paths $\mathcal{C}$ and $\mathcal{C}^*$, respectively, defined by a radius-vector $\mathbf{R}(l)$, where l is the path arclength.

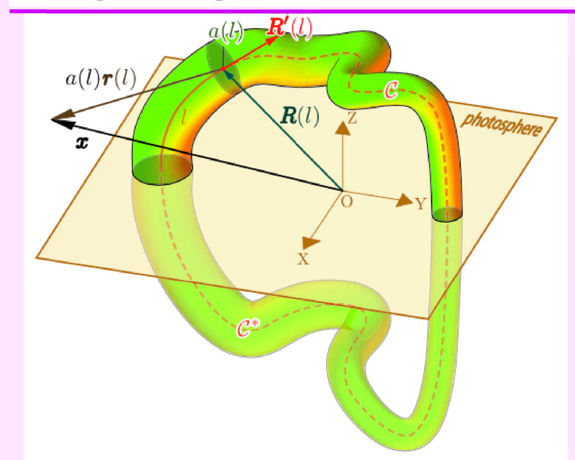

2 Magnetic field representation
$\mathbf{B} = \mathbf{B}_{\mathrm{pot}} + \mathbf{B}_{\mathrm{MFR}}$,
$\mathbf{B}_{\mathrm{MFR}} = \nabla \times \mathbf{A}_I + \nabla \times \mathbf{A}_F$,
$(\hat{\mathbf{n}}\cdot\mathbf{B}_{\mathrm{MFR}}) = 0$ at the boundary

$\mathbf{B}_{\mathrm{pot}}$ is a potential field determined from a given $(\hat{\mathbf{n}}\cdot\mathbf{B})$ at the boundary;
$\mathbf{A}_I$ and $\mathbf{A}_F$ are vector potentials defined by RBSLs from a given axis path of the MFR.

axial vector potential due to the axial electric current I

$$\boldsymbol{A}_I(\boldsymbol{x}) = \int_{\mathcal{C}\cup\mathcal{C}^*} K_I(r)\, \boldsymbol{\mathcal{R}}' \,\frac{\mathrm{d}l}{a}, \quad \left[\!\left[\frac{\mu I}{4\pi}\right]\!\right]$$

$$\boldsymbol{r} \equiv \boldsymbol{r}(l) = (\boldsymbol{x} - \boldsymbol{\mathcal{R}}(l))/a, \quad \boldsymbol{\mathcal{R}}' = \mathrm{d}\boldsymbol{\mathcal{R}}/\mathrm{d}l$$

axial flux F for a straight force-free MFR with the parabolic profile $j_{\mathrm{ax}}(\rho)$ and vanishing axial field

$$\frac{F}{\mu I a} \equiv \sigma = \frac{\pm 3}{5\sqrt{2}} \approx 0.424$$

azimuthal vector potential due to the axial magnetic flux F

$$\boldsymbol{A}_F(\boldsymbol{x}) = \int_{\mathcal{C}} K_F(r)\boldsymbol{\mathcal{R}}' \times \boldsymbol{r}\,\frac{\mathrm{d}l}{a} - \int_{\mathcal{C}^*} K_F(r)\boldsymbol{\mathcal{R}}' \times \boldsymbol{r}\,\frac{\mathrm{d}l}{a}, \quad \left[\!\left[\frac{F}{4\pi a}\right]\!\right]$$

Regularized Biot–Savart Laws (RBSLs, upgraded)

The distributions for both axial and azimuthal currents are mirrored about the boundary plane to vanish $(\hat{\mathbf{n}}\cdot\mathbf{B}_{\mathrm{MFR}})$ at the boundary.

RBSL kernels corresponding to the axial current density $j_{\mathrm{ax}} = 2(1-\rho^2)$, $[I/(\pi a^2)]$, of a straight force-free MFR with a vanishing external axial field

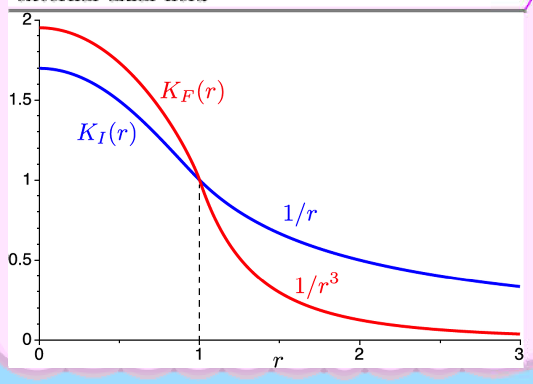

The coronal axis path $\mathcal{C}$ is represented by a cubic spline of $N+1$ equidistant control nodes (white circles) uniformly parameterized by parameter ν from 0 to N. The gray circles show evaluation nodes at which the line density of the magnetic force is calculated. The subphotospheric axis path $\mathcal{C}^*$ is a copy of $\mathcal{C}$ mirrored about a plane that locally approximates the spherical solar boundary.

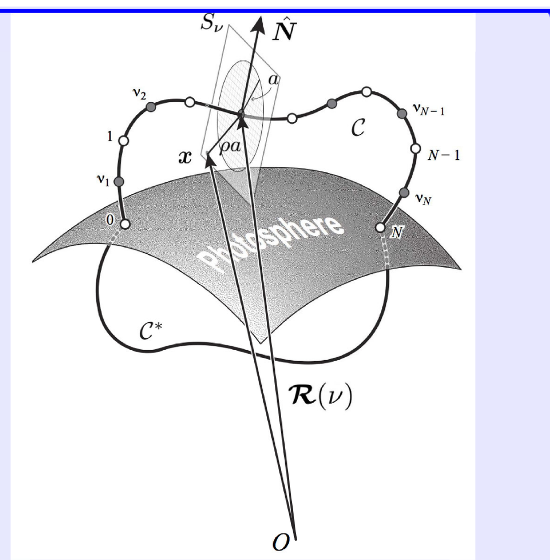

dimensionless parameter C_I

B_u is a magnetic field unit

$$I = C_I I_{\mathrm{u}}, \quad I_{\mathrm{u}} = 4\pi a B_{\mathrm{u}}/\mu$$

optimized value

$$C_I = -\sum_{\nu=\nu_1}^{\nu_N} \frac{|\boldsymbol{f}_{\nu_{\mathrm{p}}}|^2}{|\boldsymbol{f}_{\nu_{IF}}|^2} \Big/ \sum_{\nu=\nu_1}^{\nu_N} \frac{\boldsymbol{f}_{\nu_{\mathrm{p}}}^{\mathrm{T}} \boldsymbol{f}_{\nu_{IF}}}{|\boldsymbol{f}_{\nu_{IF}}|^2}$$

line density of the magnetic force

$$\boldsymbol{f}_\nu = \int_{S_\nu} [1 - (\boldsymbol{x} - \boldsymbol{\mathcal{R}}) \cdot \boldsymbol{\mathcal{R}}''] (\boldsymbol{j} \times \boldsymbol{B})\, \mathrm{d}^2\boldsymbol{x}$$

cost function

$$W = \frac{1}{N} \sum_{\nu=\nu_1}^{\nu_N} \boldsymbol{w}_\nu^{\mathrm{T}} \boldsymbol{w}_\nu,$$

$$\boldsymbol{w}_\nu = \frac{C_I^{-1} \boldsymbol{f}_{\nu_{\mathrm{p}}} + \boldsymbol{f}_{\nu_{IF}}}{|\boldsymbol{f}_{\nu_{IF}}|},$$

$$\boldsymbol{f}_\nu = C_I \boldsymbol{f}_{\nu_{\mathrm{p}}} + C_I^2 \boldsymbol{f}_{\nu_{IF}},$$

where $\boldsymbol{f}_{\nu_{\mathrm{p}}}$ and $\boldsymbol{f}_{\nu_{IF}}$ are two separate parts of $\boldsymbol{f}_\nu$ due to $\boldsymbol{j} \times \boldsymbol{B}_{\mathrm{p}}$ and $\boldsymbol{j} \times (\boldsymbol{B}_I + \sigma \boldsymbol{B}_F)$, respectively.

3 Optimization of $\mathbf{R}(\nu)$ and I

by adjusting the locations of control nodes of the axis path

2009 Feb 13 CME model : field-line structure (a) and maps of α (b) and $\log_{10} Q$ (c) in the central cross-section of the MFR before line-tied $\beta = 0$ MHD relaxation of the optimized configuration. The grayshaded $\log_{10} Q$-map is blended with the corresponding blue-red α-map.

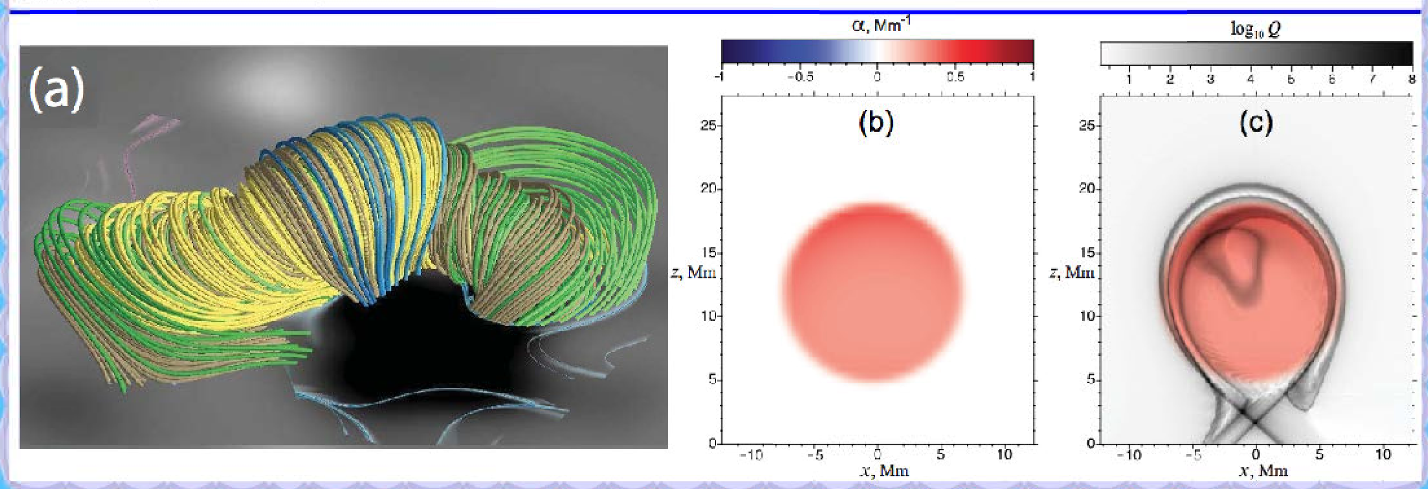

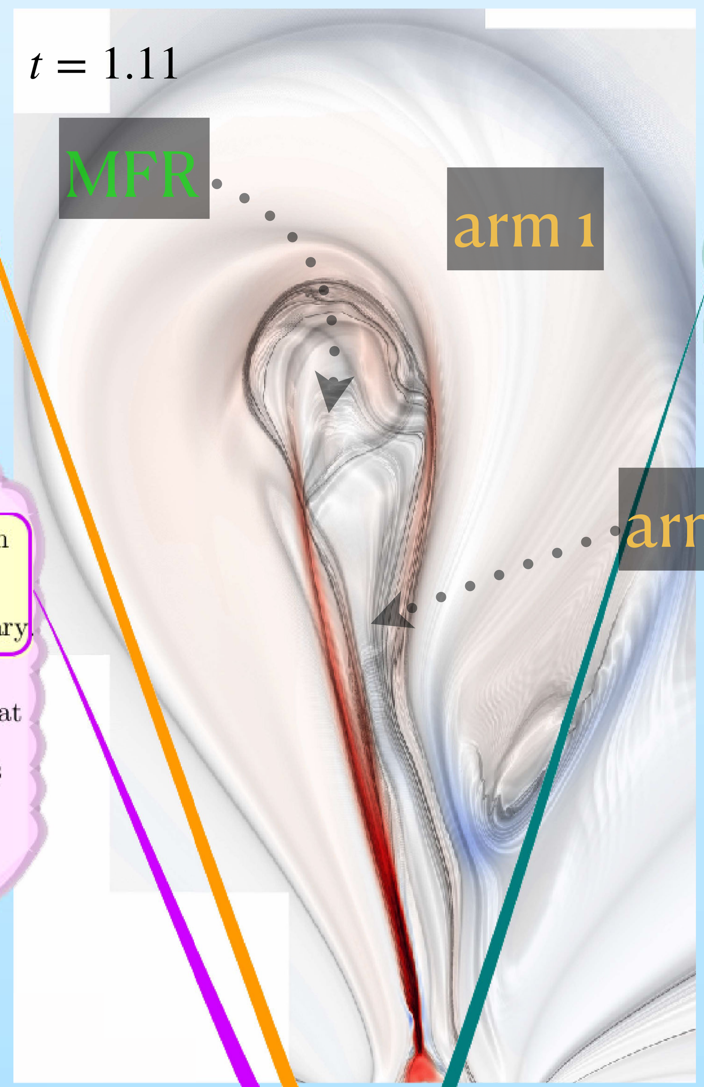

steps

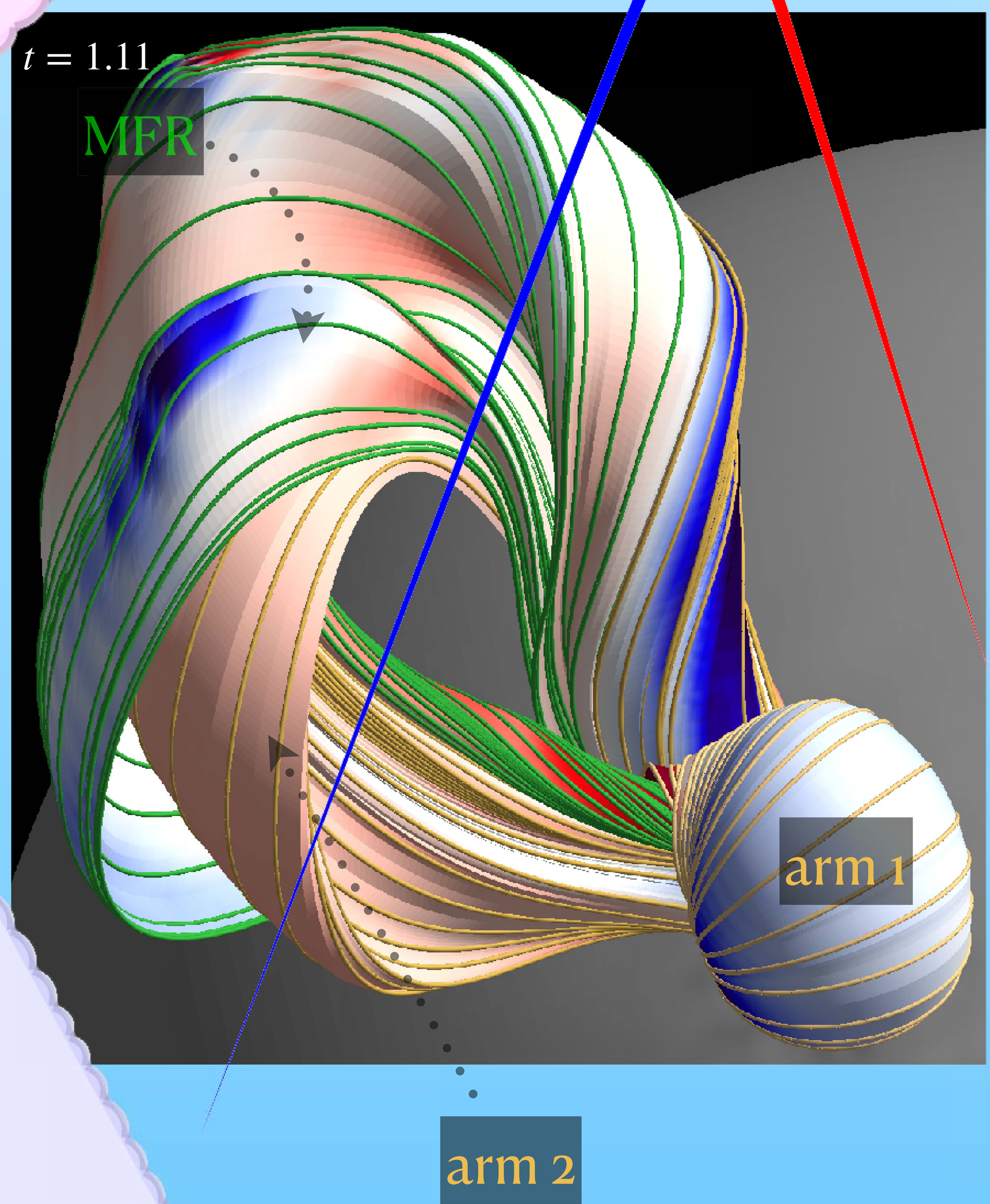

6 Analysis of the modeled eruption

based on the maps of the squashing factor Q

2009 Feb 13 CME model : Side (a) and top (c) views of the magnetic field structure during the W evolution shown here at $t = 0.64$. The shown magnetic surfaces that bound the MFR and its "arms" and the quasi-separators QS1 and QS2 are derived from the Q-map (b) in the central cross section of the configuration.

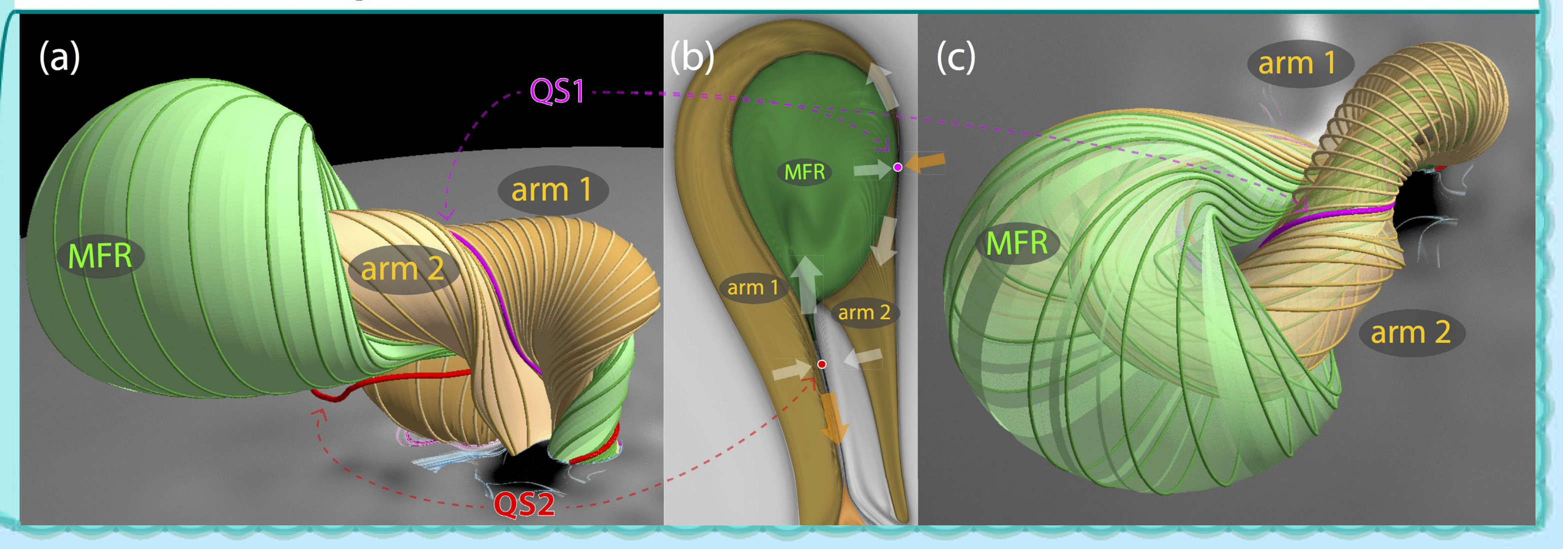

5 Helicity-pumping energization toward eruption

via cycles of the perturbation $\tilde{\mathbf{B}} = \mathbf{B}_{\mathrm{pot}} + (1+\varepsilon)\,\mathbf{B}_{\mathrm{MFR}}$ and line-tied MHD relaxation

2009 Feb 13 CME model : The evolution of the free magnetic energy W of our pre-eruptive configuration during the energization by our helicity-pumping method (solid lines). The distribution of α in the central cross-section of the configuration is shown at the beginning or end of each cycle to show how the current structure evolves during this process. For comparison, the dashed brown curve presents the decay of the free energy during the initial relaxation of the optimized RBSL MFR configuration toward the pre-eruptive configuration. The relaxation phase of the third cycle is prolonged from $t \approx 0.37$ to $t \approx 0.55$ to prove that the preliminary last cycle (dotted line) is indeed destabilizing.

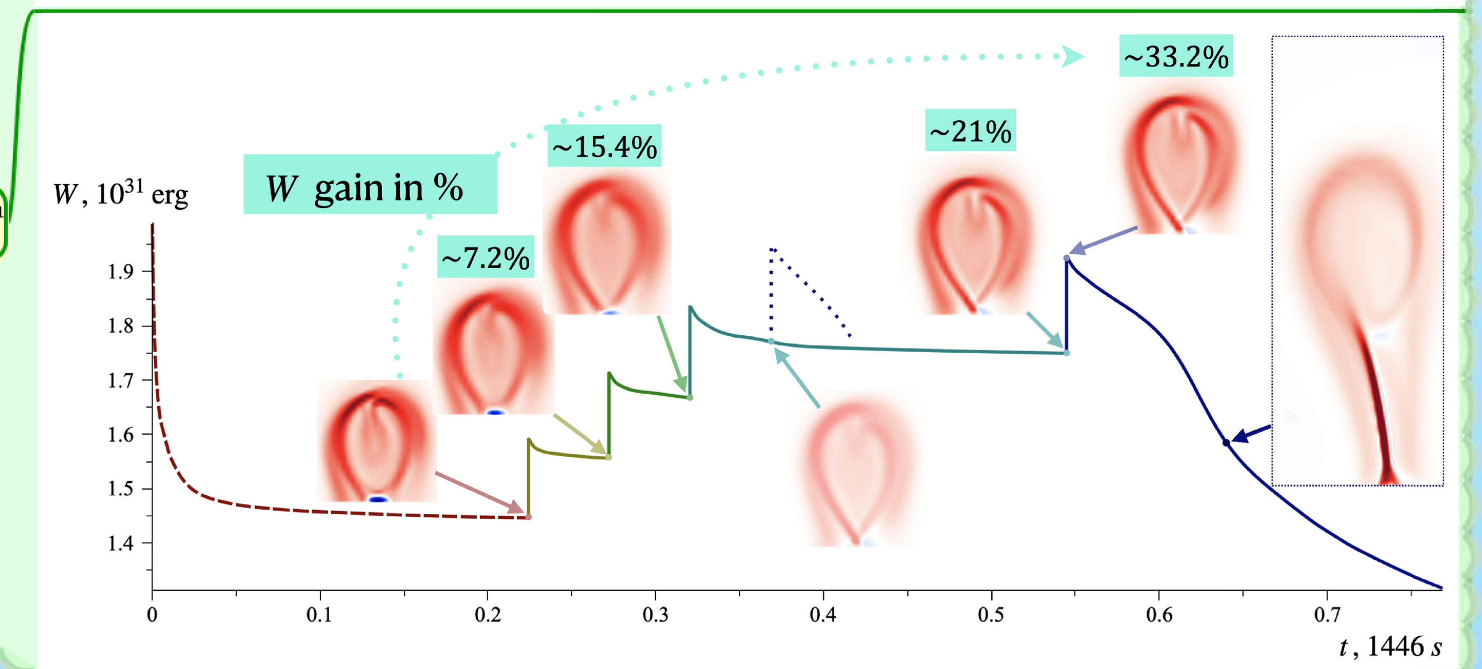

4 Line-tied zero-β MHD relaxation

of the optimized approximate RBSL MFR equilibrium

2009 Feb 13 CME model : The initial pre-eruptive equilibrium : maps of α (a) and $\log_{10} Q$ (b) in the central cross-section of the configuration whose magnetic field lines and current layers are shown in (c) and (f) (side view) and (d) and (g) (top view), respectively. Field lines of the MFR and SMA are colored in green and yellow, respectively. Isosurfaces $j/j_{max} = 0.438$ (magenta) and $\alpha/\alpha_{\min} = 0.079$ (semitransparent cyan) show the corresponding layers of direct and return currents. Panel (e) depicts representative field lines corresponding to observed morphological features (Titov et al. , 2021). The photospheric B_r distribution is shown by gray shading from white ($B_r > 0$) to black ($B_r < 0$); the overlaid high-Q lines colored in magenta (if $B_r > 0$) and cyan (if $B_r < 0$) outline the footprints of the MFR and SMA. The two quasi-separators (QS1 and QS2) described in this section are indicated in panel (b).

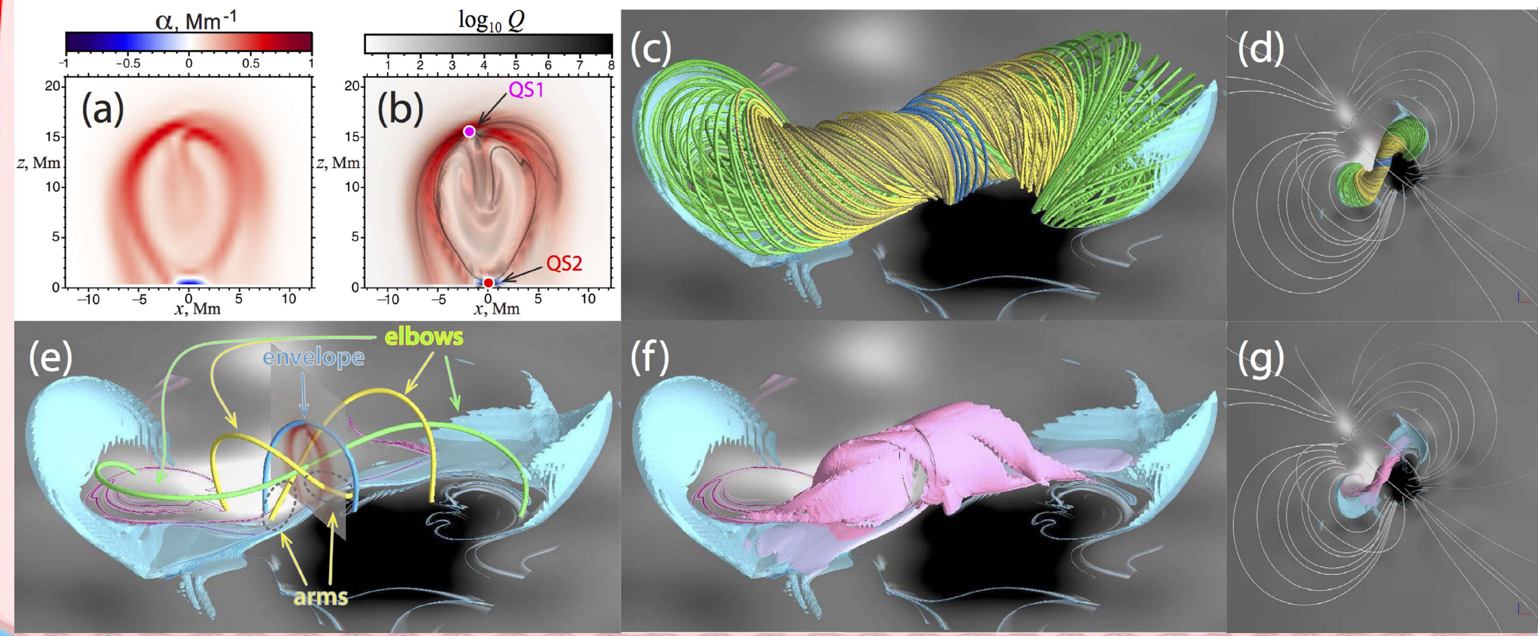

References

Titov, V. S., 2007, Generalized Squashing Factors for Covariant Description of Magnetic Connectivity in the Solar Corona, ApJ, **660**, 863

Titov, V. S., Downs, C., Mikić, Z., Török, T., Linker, J. A., and Caplan, R. M., 2018, Regularized Biot-Savart Laws for Modeling Magnetic Flux Ropes, ApJ, **852**, L21

Titov, V. S., Downs, C., Török, T., Linker, J. A., Caplan, R. M., Lionello, R., 2021, Optimization of Magnetic Flux Ropes Modeled with the Regularized Biot-Savart Law Method, ApJS, **255**, 9

Titov, V. S., Downs, C., Török, T., Linker, J. A., 2022, A Magnetogram-matching Method for Energizing Magnetic Flux Ropes Toward Eruption, arXiv:2205.03982, ApJ, under revision